C h a p t e r

5

Measuring Ocean Surface Wind from Space

Authors: W. Timothy Liu and Xiaosu Xie

This chapter summarizes the measurement of ocean surface wind vectors by scatterometers and wind speed by radar altimeters, synthetic aperture radars (SAR), and microwave radiometers. Secondary factors, other than winds, that affect radar backscatter are reviewed. Potential methods to improve wind retrieval are also discussed. Examples of recent applications using improved coverage and resolution are provided. Anticipated future technology and satellite missions are introduced.

5.1 INTRODUCTION

Just a few decades ago, almost all ocean wind measurements came from merchant ships. However, the quality and geographical distribution of these wind reports were uneven. Today, operational numerical weather prediction (NWP) also gives us wind information, but NWP depends on models, which are limited by our knowledge of the physical processes and the availability of data.

Wind is a vector quantity. Spaceborne microwave scatterometers are the only proven instruments that will give us measurements of both wind speed and direction over the ocean, under clear and cloudy conditions, day and night. They give us not only a near-synoptic global view, but also details not possible using NWP models. Such coverage and resolution are crucial to understanding and predicting the changes of weather and climate. The primary function of the radar altimeter, the SAR, and the microwave radiometer is not wind measurement, but they can give wind speed as a secondary product. Wind speeds are important in their own right, and wind speed from these sensors can be combined with directional information derived from other means.

The principles of scatterometry and scatterometer missions will be summarized in Sections 5.2 and 5.3. The number of studies on wind retrieval algorithms and their valida-tion is large. The scope of this paper does not allow a detailed review on these subjects. However, secondary factors on backscatter cause errors in wind retrieval from active sen-sors. Recent improvement in retrieval accuracy makes secondary factors timely issues; they are described in Section 5.4. Potential improvements in retrieving strong, high-resolution, and high-frequency wind vectors are discussed in Section 5.5. Wind speed measurements by various sensors are reviewed in Section 5.6. A polarimetric radiometer mission that has the potential of providing wind vectors is described in Section 5.7. Examples of current scientific applications based on the improved resolution and coverage of *QuikSCAT* are

given in Section 5.8. Future technologies are summarized in Section 5.9, and potential wind vector data available in the future are discussed in Section 5.10.

5.2   PRINCIPLES OF SCATTEROMETRY

During World War II, marine radar operators observed noise on their radar screens that obscured small boats and low-flying aircraft. They termed this noise "sea clutter." This clutter was the backscatter of the radar pulses caused by the small waves on the ocean's surface (Moore and Fung 1979). The radar operators at that time were quite annoyed by this noise, not knowing that a few decades later scientists would make important applications with what they considered noise.

Scatterometers send microwave pulses to the Earth's surface and measure the power backscattered from the surface roughness. The roughness may describe the characteristics of polar ice or vegetation over land. Over the ocean, which covers over three-quarters of the Earth's surface, the backscatter is largely due to the small centimeter-scale waves on the surface. The idea of remote sensing of ocean surface winds was based on the belief that these surface ripples are in equilibrium with the local wind stress. At incident angles greater than 20°, the radar return is governed by Bragg scattering, and the backscatter increases with wind speed, as confirmed by the aircraft experiment of Jones et al. (1978).

The backscatter is governed by the in-phase reflections from surface waves. For a smooth surface, the radar receives no return when viewing at an angle. But, as the surface roughness increases, backscatter occurs as constructive interference of scattering from periodic structures in the surface roughness. The backscatter depends not only on the magnitude of the wind stress but also the wind direction relative to the direction of the radar beam (azimuth angle). The capability of measuring both wind speed and direction is the major characteristic of the scatterometer.

Because the backscatter is symmetric about the mean wind direction, observations at many azimuth angles are needed to resolve the directional ambiguity. A scatterometer that measures only at two orthogonal azimuth angles, such as *Seasat* (see Section 5.3), always includes wind solutions of nearly equal magnitude and 180° apart. Because of the uncertainties in the wind retrieval algorithm and noise in the backscatter measurements, the problem with this directional ambiguity was not entirely eliminated with additional azimuthal looks in the scatterometers launched after *Seasat*. A median filter iteration technique initialized by the wind-direction solution closest to the NWP wind field has been commonly used to remove the directional ambiguity (e.g., Shaffer et al. 1991; Gonzales and Long 1999).

Theoretical studies of the relationship between wind and backscatter based on laboratory data have a long history. Plant (1990) and others have reviewed the theory of Bragg scattering, upon which scatterometer wind retrieval is based. However, these theoretical or dynamic-based relationships are not sufficient for operational wind retrieval in open oceans. The geophysical model function (GMF), from which ocean surface wind vectors are retrieved from the observed backscatter in the form of a normalized radar cross section (σ_o), is largely based on empirical fits of data (e.g., Stoffelen and Anderson 1997; Wentz and Smith 1999).

Because the capillary waves, which determine backscatter, are generated by stress, the approach of relating σ_o directly to measurements of surface stress has been developed (e.g., Liu and Large 1981; Weissman and Graber 1999). The geophysical data product of the scatterometer is defined as the equivalent neutral wind (ENW) (Liu and Tang 1996), because stress is uniquely related to ENW, while the relations between stress and the actual winds depend on atmospheric stability. However, there are far more wind than stress

measurements over oceans for development of GMF. In the calibration of GMF, the wind and stratification parameters measured at certain heights above the ocean surface are used to compute the surface stress and roughness parameter through a turbulence transfer model in the atmospheric surface layer (e.g., Liu et al. 1979). From the stress and roughness parameter, ENW is computed assuming neutral stability. The backscatter has also been related to pressure gradient or geostrophic winds, which may be more coherent over the scatterometer footprint than surface winds (Brown 2000).

5.3 SCATTEROMETER MISSIONS

Historically, the European Space Agency (ESA) used C-band (5 GHz) scatterometers, but the National Aeronautics and Space Administration (NASA) preferred Ku-band (14 GHz) scatterometers. A higher frequency is more sensitive to shorter surface waves. The Ku-band is more sensitive to wind variation at low winds but is more subject to atmospheric effects and rain contamination. The major characteristics of four scatterometers are summarized in Figure 5-1.

Spaceborne Scatterometers
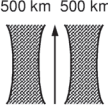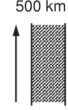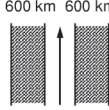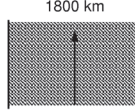
	SEASAT	ERS-1/2	NSCAT	QuikSCAT
Frequency	14.6 GHz	5.3 GHz	13.995 GHz	13.402 GHz
Scan Pattern				
Polarization	V-H, V-H	V ONLY	V, V - H, V	V, H
Inc. Angle	22°-55°	18°-47°, 24°-57°	18°-57°, 22°-63°	46°, 54°
Beam Resolution	Fixed Doppler	Range Gate	Variable Doppler	Spot
Resolution	50 km	50 km	25 km	25/12.5 km
Swath	500 km 500 km	500 km	600 km 600 km	1800 km
Daily Coverage	Variable	41%	77%	93%
Dates	6/78 – 10/78	8/91-1/01	8/96 – 6/97	6/99 +

Figure 5-1   Characteristics of spaceborne scatterometers.

NASA launched a scatterometer on the Seasat Mission in June 1978. Four fan-beam, dual-polarized antennae, oriented at 45° and 135° to the spacecraft subtrack, illuminated two 500-km swaths, one on each side of the spacecraft, providing wind vectors at 50-km resolution. However, only one side was in operation most of the time, covering less than 40% of the global ocean daily. The incident angle varied from 25° to 55°. The accuracy of the backscatter is about 0.7 dB. The two orthogonal azimuth angles were not able to resolve the wind direction unambiguously. *Seasat* failed in October 1978. Pierson (1983) gave a good summary of early scatterometer efforts.

A scatterometer was launched by ESA on the first *European Remote Sensing* (*ERS-1*) satellite in August 1991, and it was followed by an identical instrument on *ERS-2*, which was launched in April 1995 and put into operation in 1996. The ERS scatterometers scanned a 500-km swath on one side of the satellite, and measured at three azimuth angles—45°,

90°, and 115°—with vertical polarization only. They provided winds over only 41% of the global ocean daily. The incident angle varied from 24° to 57° for the fore and aft beams and from 18° to 47° for the midbeam. The backscatters had 50-km spatial resolution but were sampled at 25 km.

The NASA Scatterometer (NSCAT) was launched in August 1996 on the first Japanese *Advanced Earth Observing Satellite (ADEOS-I)*, which was later renamed *Midori*. The six fan-beam antennae provided 600-km swaths on both sides of the spacecraft, covering 77% of the global ocean at 25-km resolution daily. The accuracy of backscatter was 0.2 dB. The antennae made observations at 45°, 115°, and 135° azimuth angles to the spacecraft track. The fore and aft beams measured only at vertical polarization, with incident angle varying from 22° to 63°, while the midbeam measured at both vertical and horizontal polarization, with incident angle varying from 18° to 57°. The unexpected destruction of the solar array caused the early demise of NSCAT after it had returned nine months of data.

NASA launched SeaWinds, a Ku-band scatterometer with a new design, on *QuikSCAT* in 1999. It used pencil-beam antennae in a conical scan and had a continuous 1,800-km swath that covered 93% of the global ocean in a single day. The standard wind product had 25-km spatial resolution, but special products with 12.5-km resolution were produced for selected regions. It measured horizontally and vertically polarized backscatter at 46° and 54° incident angles, respectively. An identical SeaWinds instrument was launched on Japanese spacecraft *ADEOS-II* in December 2002. *ADEOS-II* suffered severe power loss from the solar panel on 23 October 2003 and was put in an anomaly status, with no data returned from SeaWinds since that time. The older scatterometer aboard *QuikSCAT* will be referred to as QuikSCAT, and the newer scatterometer aboard *ADEOS-II* will be referred to as SeaWinds, hereafter.

A series of advanced scatterometers (ASCAT) are planned to be launched on the European meteorological platform (METOP), starting in 2006, with spatial resolution of 50 km (Figa-Saldana et al. 2002). Their fan-beam antennae will cover two 550-km swaths that are separated from the satellite ground trace by about 360 km. They will operate at C-band, with incident angles ranging from 25° to 65°.

5.4   SECONDARY FACTORS

While wind is the primary factor in the changes of backscatter measured by a scatterometer, other secondary factors, such as atmospheric stability (5.4.1), sea surface temperature (SST) (5.4.2), surface film (5.4.3), surface current (5.4.4), and rain (5.4.5), may also affect scatterometer measurement, and may cause errors in wind retrieval. Because these factors are related to each other, the separation of their small and independent effects on wind retrieval is not an easy task. In many cases, coincident measurements of these factors are not available to make the correction in scatterometer wind retrieval. With the increasing accuracy of scatterometer wind measurements, understanding and quantifying such effects are becoming increasingly important. The studies of relations between backscatter and these factors have become scientific fields in their own right.

5.4.1   Atmospheric Density Stratification

The geophysical product of a scatterometer is ENW, a theoretical parameter, because ENW is uniquely related to the surface stress measured by the scatterometer (Liu and Tang 1996). The relation between ocean surface stress and actual wind at a reference height depends on

atmospheric stability. Atmospheric stability depends on both wind shear and density stratification. Even for uniform winds, the scatterometer should observe higher ENW (or stress) over warmer water (more unstable), according to turbulence theory. Liu and Large (1981) first examined the stability-dependent discrepancies in the Seasat scatterometer GMF. Liu (1984) found that the error (compared with collocated buoy measurements) of ENW from the Seasat scatterometer is a function of atmospheric stability, even after the effect of SST is removed. Quilfen et al. (2001) found a seasonal cycle in the ensemble mean differences between ERS-2 winds and buoy winds that match the seasonal cycles of coincident sea-air temperature differences and significant wave height. They did not separate the independent effects of various factors. The stability dependence observed in scatterometer winds may be caused by residual stability effects that are not effectively removed in computing the ENW used in the calibration. The cause of error may also be that the maintenance of surface capillary waves depends on atmospheric stability, as suggested by Wu (1991).

5.4.2   Sea Surface Temperature

The sea surface temperature (SST) may affect capillary waves and backscatter through the viscosity effect (Lleonart and Blackman 1980). Liu (1984) showed that the difference between collocated wind speed measured by the Seasat scatterometer and buoys is a function of SST, independent of the variation of atmospheric stratification, particularly at low wind speeds (<6 m/s). Ebuchi (1997) found that the backscatter measured by ERS scatterometers is a function of SST, but concluded that the dependence is not caused by the temperature dependence of viscosity or atmospheric stability. The effects of SST on backscatter have been studied extensively in laboratory and ground-based experiments, but with strong disagreement in trends of magnitude (e.g., Keller et al. 1989; Zheng et al. 1997).

5.4.3   Natural Surfactants

The backscatter attenuation caused by accidental oil-spills in the ocean has long been observed (e.g., Krishen 1973). The effects of the more ubiquitous natural surface film caused by biological productivity are less established. The surface films damp surface short-waves through surface tension, affecting microwave backscatter (e.g., Barger et al. 1970; Alpers and Huhnerfuss 1989). Such damping was studied in a series of aircraft experiments over the North Sea over the past two decades (e.g., Huhnerfuss et al. 1978; Gade et al. 1998). The effect has been widely inferred in space-based synthetic aperture radar observations (e.g., Clemente-Colon and Yan 1999; Liu et al. 2000a; Lin et al. 2002). The effects of surface films on space-based scatterometer observations have been more elusive. Lin et al. (2003a) were the first to show the surfactant effect on QuikSCAT observations and Hashizume and Liu (2004) examined the correlation between QuikSCAT wind errors and surfactant associated with ocean biological productivity over global oceans on intra-seasonal and seasonal time scales.

5.4.4   Surface Current

Wind stress depends on wind shear, or the difference between the wind vector near the surface and the surface current. Surface current has been included in the formulation of bulk parameterization of stress (e.g., Liu et al. 1979). The magnitude of ocean current is assumed to be negligible compared with wind, both in experimental determination of the

drag coefficient and in developing the wind retrieval algorithm for the scatterometer. The importance of surface current feedback on the determination of stress in the tropical ocean, where the current is relatively strong compared with the winds, was studied by simulation using ocean general circulation models (e.g., Pacanowski 1987) and through observations (Kelly et al. 2001). Sharp changes in the direction of ocean surface current occur over ocean eddies and fronts; their strong and clear effects on the scatterometer measurement have been observed by Cornillon and Park (2001) and Polito et al. (2001).

5.4.5   Rain

There are clear indications that rain affects wind retrieval because of scattering by raindrops in the atmosphere and roughening the ocean surface by falling rain (Sobieski and Bliven 1995; Weissman et al. 2002). Considerable effort is being directed in producing rain flags for QuikSCAT data (e.g., Huddleston and Stiles 2000; Portabella and Stoffenlen 2002). The energy received by QuikSCAT includes both backscatter and radiance. The radiance is usually viewed as noise in wind retrieval. Jones et al. (2001) and Boukabara et al. (2002) were able to derive coincident rain rate from the radiance observed by QuikSCAT and to give a better quantification of the rain effect than a simple rain flag.

QuikSCAT is the only scatterometer that does not fly with a rain sensor. All past scatterometer missions included microwave radiometers that provided coincident rain measurements, and all future missions will do the same. The level of rain at which wind retrieval becomes invalid is under study (e.g., Stiles and Yueh 2002). Useful information is lost if all winds retrieved under rainy conditions are discarded. Better methods are needed to retrieve accurate wind vectors under rainy conditions (e.g., Yueh et al. 2001, 2003).

5.5   POTENTIAL IMPROVEMENT

There are strong operational and research needs in monitoring tropical cyclones and coastal oceanic processes (Liu et al. 2001). Tropical cyclones (TC) at sea are hazardous to ships, and their landfall is devastating to human livelihood. A large population lives near the coast, and coastal oceans are the most productive part of global oceans. Tropical cyclones are driven by strong winds, and the nutrients in coastal oceans are controlled by wind-driven upwelling. Coastal processes and marine storms are highly variable. Both problems require vector winds with high resolution (spatial and temporal). In regard to spatial resolution, Liu et al. (1998a) demonstrated that spaceborne scatterometers, even the standard data, hold a clear edge over operational NWP products. There are also debates on the scatterometer's ability in measuring strong winds in storms. The potential of scatterometers for measuring strong winds, winds in higher resolution, and winds at higher frequency is discussed in Sections 5.5.1, 5.5.2 and 5.5.3, respectively.

5.5.1   High Intensity

The accuracy of high winds is important in the studies of marine storms. Theoretical studies (e.g., Donelan and Pierson 1987) suggested high-wind saturation in deriving winds from backscatter. Such limitations have not been clearly observed. Donnelly et al. (1999) measured backscatter on an aircraft flown over hurricanes. When the backscatter coefficients in dB (logarithmic scale) are plotted against wind speed, the curve appears to become flat at wind speeds above 20 m/s. The results appear to support the theoretical

postulation of backscatter saturation at high winds. However, sensitivity can still be observed in linear plots. In a similar aircraft experiment, Yueh et al. (2000) demonstrated that horizontal polarization is more sensitive than vertical polarization at high winds; there was still significant variation of backscatter as a function of wind at wind speeds higher than 35 m/s. Wentz et al. (2001) showed that the backscatter measured by QuikSCAT is sensitive to wind variation at wind speeds as high as 50 m/s, under clear-sky conditions. Yueh et al. (2001) showed that the backscatter measured by QuikSCAT over TC is sensitive to the variation of hurricane-scale (up to 50 m/s) winds at various rain rates.

Significantly higher winds than measured by oceanic buoys (a maximum of 23 m/s) are routinely measured in storms over regions of thousands of square km and over many hours' duration. The inability of buoy instruments and NWP products, which serve as calibration standards, to capture such high winds led to errors in scatterometer winds (Zeng and Brown 1998). The errors could be corrected by winds derived from a planetary boundary layer model, as suggested by Brown and Zeng (2001).

5.5.2   High Spatial Resolution

The current standard 25-km resolution wind product of QuikSCAT is derived from an ellipsoidal instantaneous antenna footprint with characteristic dimensions of 25 × 35 km (a so-called "egg"). The backscatters with footprint center falling within a 25-km grid were averaged to give a wind-vector solution. The grid size that determines the spatial resolution was selected to reduce noise without aliasing. Using onboard filtering, the egg can be divided into smaller, contiguous "slices" having characteristic dimensions of about 6 × 25 km (Spencer et al. 2000). Smaller grid size and high spatial resolution can be achieved, in principle, by using "slices" instead of "eggs." A limited amount of surface wind data at 12.5-km resolution has been produced from QuikSCAT and successfully applied in studies of tropical cyclones (Liu et al. 2000), coastal eddies (Hu and Liu 2002), and coastal wind jets (Hu and Liu 2003). These high-resolution winds are found to have bias and root-mean-square differences similar to standard data when compared with off-shore buoy measurements, but have slightly larger values when compared with coastal buoys (within 10–30 km from shore) (Tang et al. 2004).

Long et al. (1993) developed a technique to produce resolution-enhanced backscatter (with 8-km resolution) by combining multi-pass data and successfully applied this to land and ice studies, when temporal resolution was not critical. The dense sampling in QuikSCAT slice data makes it possible to apply the resolution-enhancement technique to a single pass of data, thus increasing the spatial resolution of ocean surface winds without sacrificing the temporal resolution (Long 2001). More vigorous evaluations are needed on the amount of accuracy degradation of these winds caused by the gaining of spatial resolution.

5.5.3   High Frequency

High frequency wind fields can be obtained using satellites in low Earth orbits (e.g., 800 km), either with a constellation of instruments in polar orbits, or with a single instrument in low-inclination orbit. It can also be acquired by flying a scatterometer at a high attitude that optimizes the swath width, but below the hostile radiation environment (e.g., 1,500 km).

With the launch of *ADEOS-II* in December 2002, two identical scatterometers flew in tandem and returned data for approximately six months. QuikSCAT measured ocean surface vector winds around 6 A.M. and 6 P.M. local time, while SeaWinds measured around 10:30 A.M. and 10:30 P.M. With both instruments operating in tandem, the coverage of the

global ocean exceeded 60% in 6 hours and 90% in 12 hours. In comparison, 90% coverage with QuikSCAT or SeaWinds alone required 24 hours of sampling (Figure 5-2). The average revisit interval for the single QuikSCAT mission (or, equivalently, the single SeaWinds mission) decreased with increasing latitude from about 19 hours at the equator to about 10 hours at 60° latitude. For the tandem QuikSCAT/SeaWinds sampling pattern, the average revisit interval decreased from about 9 hours at the equator to about 6 hours at 60° latitude. The tandem mission reduced the average revisit time by approximately 40% at Earth locations and helped to meet the 6-hour operational updating requirement of meteorological centers. It filled the approximately 10% daily spatial gaps, which is important for monitoring small and moving hurricanes. Liu (2003) gave an overview of the scientific opportunities made possible by flying scatterometers in tandem.

Figure 5-2 shows that if wind vectors can be derived from WindSat (section 5.7) with sufficient accuracy, the temporal sampling of winds by QuikSCAT will improve slightly in the subtropical oceans. We do not know the crossing time of ASCAT at this moment, but there is a possibility that by combining ASCAT observations with those of other sensors, the temporal resolutions of ocean surface wind vector will be improved.
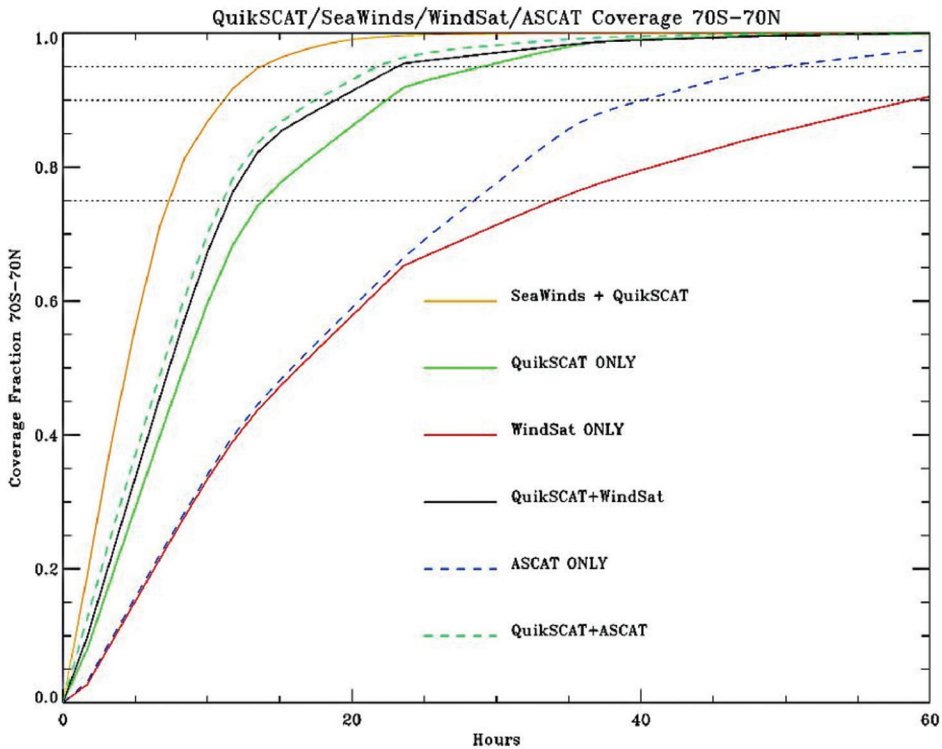

Figure 5-2   Fractional coverage between 70° latitudes as a function of time by each mission alone and when flying in tandem.

5.6   WIND SPEED

Both the microwave altimeter and SAR are similar to the scatterometer in the sense that they are active sensors that send microwave pulses to the Earth's surface and measure the backscattered power. The microwave radiometer is a passive sensor, observing the radiance from the Earth and its atmosphere. A good perspective on wind retrieval by these sensors can be gained from the special issue on "Remote Sensing of Marine Winds," *Canadian Journal of Remote Sensing,* Vol. 28, No. 3, June 2002.

5.6.1   Altimeter

While the scatterometer views at oblique angles, the altimeter views at nadir (very small incident angles). At nadir, the backscattered energy is a result of specular reflection (the wavelets serve as small mirrors), and the backscatter is not sensitive to wind direction (Barrick 1974). Because the instrument is not scanning, data are only available at very narrow (2 km) repeated ground-tracks. The coverage of altimeters is poor compared with the scatterometer and the microwave radiometers. Altimeters were flown on *Seasat* and ERS spacecraft described in Section 5.3. *Geosat,* which was in operation between 1985–1989, was a dedicated altimeter mission. There are other missions in operation with altimeters onboard, such as *TOPEX/Poseidon* launched in 1992, *Geosat* Follow-on launched in 1998, *JASON-1* launched in 2001, *ENVISA* launched in 2001, and *ICESat* launched in 2003. The proposed Wide-Swath Ocean Altimeter (WSOA), with a 200-km swath, may improve the coverage (Fu 2003).

Although poor coverage hinders atmospheric or oceanographic applications using altimeter winds, as compared to applications of wind speeds from scatterometer, radiometer, and SAR, the number of studies on the altimeter wind retrieval algorithm is much larger (over 20 papers have been published). The reason is, perhaps, that the algorithm, first used by Brown et al. (1981), is a simple empirical relation between σ_o and wind speed or the logarithm of wind speed. It has been continuously updated by better data fits with new statistical procedures and ever-improving calibration data (e.g., Chelton and McCabe 1985; Chelton and Wentz 1986; Witter and Chelton 1991; Carter et al. 1992; Young 1993). Many more algorithm studies were performed to add secondary effects related to waves (e.g., Glazman and Pilorz 1990; Glazman and Greysukh 1993; Monaldo and Dobson 1989; Dobson et al. 1987; Lefevre et al. 1994; Gower 1996; Hwang et al. 1998). Despite all of this algorithm development the accuracy of wind retrievals has not improved significantly.

Caution is needed when using altimeters to characterize climatological changes in ocean surface wind speed. There is no consistent effort to calibrate and to maintain the long-term accuracy of wind speed retrieval because *TOPEX* was not designed to provide ocean surface winds. The accuracy of wind retrieval may be sacrificed for the stability of other parameters, such as significant wave height.

5.6.2   Synthetic Aperture Radar

A SAR looks perpendicular to the spacecraft path at only one azimuth angle and cannot resolve wind direction like the scatterometer. The main objective of SAR is to provide high-resolution imaging of the Earth's surface. SAR has spatial resolutions that are much better than scatterometers, but the high resolution also introduces higher uncertainties in accuracy caused by secondary factors that affect surface roughness. The instrument and the data

processing procedure are much more complicated than the scatterometer, and calibration difficulties have been serious. The scatterometer GMF has been used to relate the σ_o measured by SAR to wind speed. However, a particular value of σ_o may correspond to a range of wind speeds, depending on the angle between the radar look direction and the wind direction. Hence, in order to perform the wind speed inversion with the GMF, the wind direction must first be specified. Whether the *a priori* wind direction information is derived from the orientation of km-scale structure in the SAR image, or from operational NWP models, the spatial scales are much coarser than σ_o. The km-scale structures in the SAR image are believed to be caused by atmospheric boundary rolls (Thompson et al. 1983). The theory on the dynamics of these rolls has been explained by Brown (1970, 2002) and others; they are present only under unstable conditions.

The SAR on *Seasat* and *ERS-1* and *-2* had a spatial resolution of approximately 30 m and swath width of 100 km. The narrow swath width and the sporadic operation prevented global monitoring of ocean surface wind. Gerling (1986) demonstrated the feasibility of deriving wind information from the Seasat SAR. Vachon and Dobson (1996) validated the wind speeds derived from the ERS-1 SAR after careful calibration of ERS-1 radar return. They used GMF developed for the ERS-1 scatterometer, and obtained *a priori* wind direction from the orientation of the low wavenumber structure in the SAR image. The recalibrated ERS SAR data have been used to retrieve wind speeds in coastal and inland waters (e.g., Lehner et al. 1998; Korsbakken et al. 1998).

Radarsat-1, which was launched in 1995, can operate in a ScanSAR mode with a spatial resolution of 100 m and a 500-km wide swath; this instrument is the closest to providing continuous global coverage. Radarsat measures at C-band and horizontal polarization, but the GMF for ERS scatterometers is for C-band and vertical polarization. Monaldo et al. (2001) converted the ERS-1 scatterometer GMF from vertical polarization to horizontal polarization and, using *a priori* directional information from operational NWP, successfully derived wind speed from Radarsat. Katsaros et al. (2000) demonstrated the use of Radarsat wind data to study marine storms. The Advanced Synthetic Aperture Radar (ASAR) launched on *Envisat* is also capable of ScanSAR operation. More reports on applications of SAR can be found in *Johns Hopkins APL Technical Digest*, Vol. 21, No. 1, 2000.

5.6.3   Microwave Radiometer

Ocean surface wind speed can also be derived from the radiance observed by a microwave radiometer. It is generally believed that wind speed affects the surface emissivity indirectly through the generation of ocean waves and foam (Hollinger 1971; Wilheit 1979). Radiometers designed to observe the ocean surface operate primarily at window frequencies, where atmospheric absorption is low. To correct for the slight interference by tropospheric water vapor, clouds, and rainfall, and, to some extent, the effect of sea surface temperature, radiances at frequencies sensitive to sea surface temperature, atmospheric water vapor, and liquid water are also measured (Wentz 1983). Wentz (1992) first showed the wind direction sensitivity in SSM/I measurements, suggesting the vector-wind measuring potential of passive microwave sensors (see Section 5.7).

Microwave radiometry has a much longer history than active microwave sensors. Ocean surface wind speeds were derived from the Scanning Multichannel Microwave Radiometer (SMMR) on *Seasat* and *Nimbus-7* launched in 1978 (Wilheit and Chang 1980). The Special Sensor Microwave/Imager (SSM/I), the first of which was launched in 1987 on the Defense Meteorological Satellite Program (DMSP) satellite, provided major improvements in wind speed availability. A linear regression relating the surface wind speed to brightness

temperatures measured by SSM/I was published by Goodberlet and Swift (1989), drawing on the results of Lo (1983). Wentz (1997) used a more physical retrieval algorithm, and their wind products were evaluated by comparison with buoy data by Mears et al. (2001) and with NWP products by Meissner et al. (2001). Several DMSP satellites with SSM/I onboard have been in orbit at the same time, providing continuous global coverage since July 1987. The Advanced Microwave Scanning Radiometers (AMSR) onboard *ADEOS-2* and NASA spacecraft *Aqua* measure winds at higher resolutions.

The wind speed from SSM/I has been combined with surface wind data from a numerical model through a variational method to produce wind vector fields at 6-hour intervals and at 1° by 1° resolution (Atlas et al. 1996). These large-scale wind fields over the tropical Pacific were evaluated by Busalacchi et al. (1993) by comparing the data with operational NWP products and interpolated wind fields from ship measurements and cloud motions. The SSM/I wind fields were found by Liu et al. (1996) to generate more realistic anomalous ocean cooling in an ocean general circulation model (GCM) when compared with the results simulated by the same model but forced by NWP winds. The SSM/I wind fields have more structure and energy than NWP winds, but have the same directional characteristics as the NWP winds.

5.7 WINDSAT

WindSat is a polarimetric microwave radiometer developed by the US Navy and the National Polar-orbiting Operational Environmental Satellite System (NPOESS) Integrated Program Office (IPO). It was launched in January 2003. The objective of the WindSat mission is to test the capability of polarimetric microwave radiometry to measure the ocean surface wind vector from space. WindSat will also serve as a risk reduction program for the Conical Microwave Imager Sounder (CMIS) to operate on the NPOESS in the post-2010 time frame.

In polarimetric radiometry, four parameters of the Stokes vector are measured to fully characterize the polarization properties of the sea surface emission. The first two Stokes parameters correspond to vertically and horizontally polarized brightness temperatures, which are being measured by SSM/I and AMSR on *Aqua* and *ADEOS-II*. The third and fourth Stokes parameters characterize the orientation and ellipticity of the polarized radiation. Several airborne experiments (Yueh et al. 1995, 1997, 1999; Skou and Laursen 1998; Piepmeier and Gasiewski 2001) demonstrated that the microwave emission from the ocean surface varies not only as a function of wind speed, but also as a function of wind direction. However, the sensitivity to wind direction is degraded in low winds (<7 m/s) and under cloudy and rainy conditions. The first two Stokes parameters can be characterized by cosine functions of sea surface wind direction and the third and fourth Stokes parameters by sine functions. The third and fourth Stokes parameters are fairly insensitive to cloud, and hence provide a promise for nearly all-weather observation capability of wind vector using passive microwave radiometry.

The WindSat radiometer system consists of a conical scanning antenna illuminated by feedhorns operating at 6.8, 10.7, 18.7, 23.8 and 37.0 GHz frequencies. The 10.7, 18.7 and 37.0 GHz radiometer channels provide fully polarimetric measurements of all four Stokes parameters of ocean surface emission, while the 6.8 and 23.8 GHz channels for sea surface temperature and atmospheric water vapor retrieval are non-polarimetric with vertically and horizontally polarized brightness temperature observations. The WindSat swath width is about 1,400 km, similar to that from the SeaWinds inner antenna beam, and provides more than 83% global coverage within a day. The WindSat antenna is a 1.8-m diameter parabolic

reflector, similar to the size of AMSR. The WindSat footprint resolution is about 12 km at 18.7 GHz, which is about a factor of three smaller than the footprint size of SSM/I. The spatial resolutions of WindSat and SeaWinds are comparable.

5.8   SCIENCE APPLICATIONS

There have been a large number of applications of scatterometer data; the major papers are collected in special volumes of the *Journal of Geophysical Research* (e.g., Vol. 87, C5, 1982; Vol. 88, C3, 1983; Vol 103, C4, 1998; Vol. 104, C5, 1999). Papers on NSCAT were collected in a compendium published by the American Geophysical Union in 1999, and a second compendium, including applications of QuikSCAT data, was published in 2004. Liu (2002) also gave a review of scientific applications of scatterometer data. In this section, only a few examples of recent studies using the improved coverage and spatial resolution will be discussed. The coverage of the scatterometer provides the synoptic view of wind field over the global oceans and contributes to operational NWP (Section 5.8.1). The improved coverage also makes it possible to study ocean moisture advection (Section 5.8.3) and monitor El Niño precursors (Section 5.8.4). The high spatial resolution allows more accurate computation of differential quantities of winds, such as divergence and curl, which are important in the studies of tropical cyclones (Section 5.8.2) and ocean-atmosphere coupling (Section 5.8.5).

5.8.1   Operational Numerical Weather Prediction

One of the classical applications of scatterometer wind measurement is in predicting weather through assimilation of the scatterometer data into the atmospheric general circulation model (GCM). Although the ERS-1 scatterometer was launched in 1991, the data were not operationally assimilated into GCM for NWP until 1994. All major weather forecast centers in Europe, Japan, and the US implemented the assimilation of ERS scatterometer winds between 1994 and 1997. NSCAT had only a short life span; the spacecraft failed before any NWP center could set up the system to assimilate its data. Both the European Center for Medium Range Weather Forecast (ECMWF) in the UK and the National Center for Environmental Prediction (NCEP) in the US began operational assimilation of the data in January 2002. The United Kingdom Meteorology Office and Japanese Meteorological Agency followed shortly thereafter. Atlas et al. (2001) provided a review on scatterometer impact on NWP recently. The potential of initialization of the NWP model using pressure gradients derived from scatterometer winds has also been explored (e.g., Davis 2002; Petoux et al. 2003).

5.8.2   Interplay Between Wind and Rain in Tropical Cyclones

Besides the potential use in four-dimensional assimilation by operational NWP, scatterometer and other satellite data have been widely used by marine weather and hurricane centers in analyzing and predicting marine storms (Katsaros et al. 2002; Ritchie et al. 2002). The increasing spatial resolution of scatterometer data provides increasingly detailed descriptions of small and intense weather systems, like tropical cyclones (Liu et al. 2000). Figure 5-3 shows that the 12.5-km spatial resolution allows the delineation of surface wind convergence associated with the multiple rain bands of Hurricane Floyd. The winds from
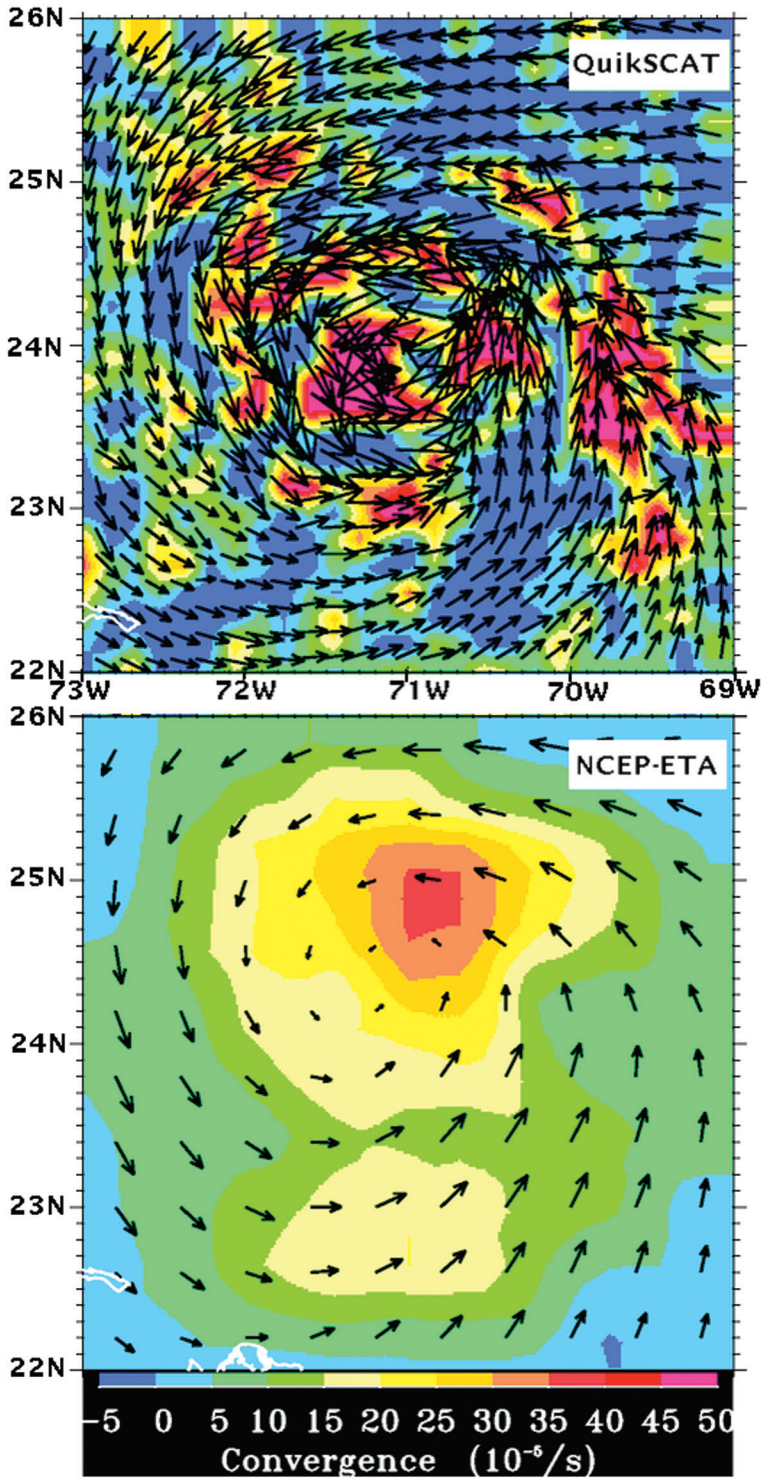
Figure 5-3   Hurricane Floyd on 13 September 1999. Black arrows representing wind vectors are superimposed on color image of wind convergence, derived from QuikSCAT (upper) and the Eta model (lower).

the Eta model are not even close to being able to resolve such rain bands. Eta is a regional NWP model producing operational wind products with the highest available spatial resolution (40 km).

Wind, the dynamic parameter, and rain, the hydrologic (latent heat) parameter, are related by the conservation principle. The influence of the ocean surface winds is not confined to the surface but is felt throughout the atmospheric column. The vertical velocity in pressure coordinate ω, at a certain level p, depends on the horizontal wind velocity u at that level and all levels below it, so that

$$\omega_p = -\int_{p_s}^{p} \nabla_h . \vec{u} \, dp \qquad (5\text{-}1)$$

where the subscript s indicates surface level. The surface wind affects ω at all levels, and ω affects the "apparent moisture sink" (Yanai et al. 1973) at each level

$$Q = -(\frac{\partial q}{\partial t} + \vec{u}\nabla_h q + \omega \frac{\partial q}{\partial p}) = c - e \qquad (5\text{-}2)$$

where q is the specific humidity, and t is the time. Q is the difference between condensation c and evaporation e, per unit mass of air. The vertical integration of Q gives the fresh water flux (F), or hydrologic forcing, at the surface

$$F = P - E = -\frac{1}{g}\int_{0}^{p_s} Q dp \qquad (5\text{-}3)$$

where g is acceleration due to gravity, E is the evaporation, and P is the precipitation at the surface. The profile of Q is conventionally expressed as the profile of diabatic heating rate per unit mass of air

$$H = LQ/c_p \qquad (5\text{-}4)$$

where c_p is the isobaric specific heat and L is the latent heat of vaporization. The equations represent the conventional way of computing the diabatic heating of the atmosphere and the hydrologic forcing on the ocean, using wind and humidity profiles from rawinsonde data (e.g., Bryan and Oort 1984). Over the ocean, rawinsonde data are sparse and products from operational NWP models are used. Provided that the variation of E is small compared with P, the horizontal pattern of F and vertical pattern of H should be comparable to the surface rain pattern and vertical rain profiles measured by Tropical Rain Measuring Mission (TRMM).

The multiple rain bands of Hurricane Floyd were clearly visible in the surface rain pattern (Figure 5-4a) and rain profiles (Figure 5-4b) measured by the precipitation radar (PR) on TRMM. The Eta model, with conventional data assimilation, cannot produce realistic rain patterns for Hurricane Floyd (Figures 5-4c and 5-4d). By simply replacing the wind divergence between 1,000 and 975 mb of the Eta assimilation with the divergence of scatterometer winds (shown in Figure 5-3) in the computation of F in Equations 5-2 and

5-3, the pattern becomes much more realistic with the appearance of the eye and more than one spiral rain band (Figures 5-4e and 5-4f). Walls of precipitation define the rain bands and locate the eye at 71.1°W, during PR overpass. The precipitation cut-off at 5 km, indicating freezing level, also agrees with observations by PR. Because Hurricane Floyd moves, model results were linearly interpolated to the time of a QuikSCAT overpass at 10:48 UT, with the spatial coordinate moving with the eye of the hurricane.
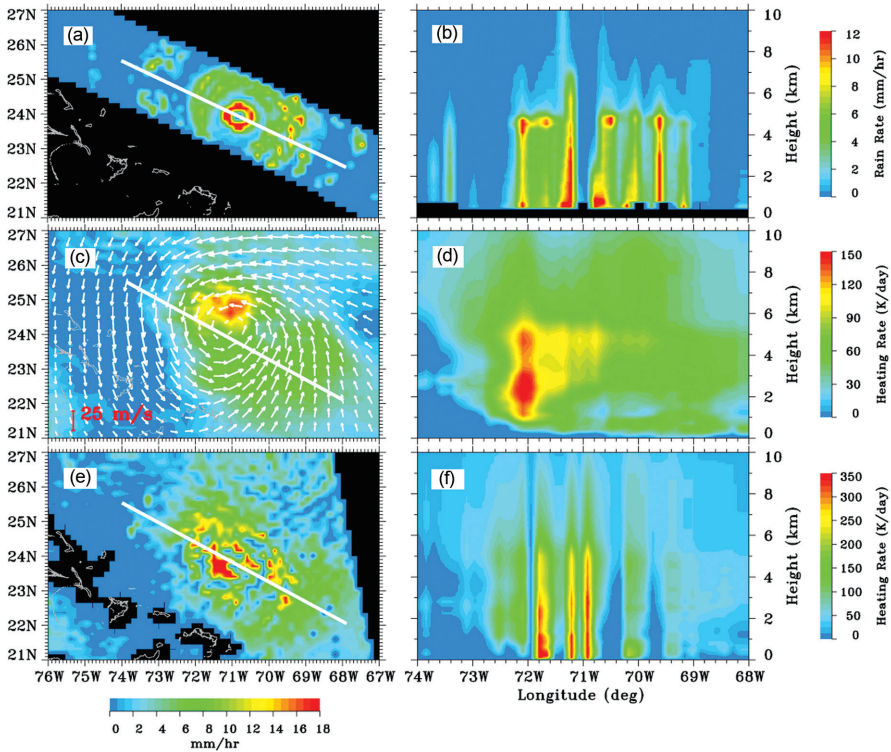

Figure 5-4   Hurricane Floyd as surface rainfall (a) and rain rate profile (b) estimated from TRMM data, as surface wind vector (white arrows) superimposed on surface water flux (c) and diabatic heating profile (d) derived from the Eta model. Panel (e) and (f) are the same as (c) and (d), except that surface wind divergence for the Eta model is replaced with QuikSCAT data. The vertical profiles are plotted along the white lines on the surface maps.

5.8.3   Oceanic Influence of Continental Rainfall

The vertically integrated moisture transport (ξ) is

$$\xi = \frac{1}{g} \int_0^{p_s} q\,\vec{u}\ dp \tag{5-5}$$

The computation of ξ requires measurement of the vertical profiles of wind vector and humidity in the atmosphere, which traditionally come from aerological (rawindsondes) data. Over oceans, rawindsonde data are sparse. Liu (1993) proposed a method to estimate ξ, using surface wind vector measured by the scatterometer and the vertically integrated water vapor (W) measured by microwave radiometer.

The method uses an equivalent velocity $\boldsymbol{u}_e$ defined by

$$u_e = \xi / W \tag{5-6}$$

where

$$W = \frac{1}{g} \int_0^{p_s} q\,dp \tag{5-7}$$

The equivalent velocity is the depth-averaged wind velocity weighted by humidity.

Since W can be accurately measured by both the operational SSM/I and TRMM Microwave Imager (TMI), the problem of measuring ξ is essentially the determination of u_e. A spaceborne scatterometer could measure the surface wind vector u_s over the global ocean. A quantitative relation between u_s and u_e is needed. The variability of humidity profile has been extensively studied by Liu et al. (1991), and the dominant mode of variability was found to peak at the top of the boundary layer. Heta and Mitsuta (1993), using W derived by Liu (1987) from the microwave radiometer on *Nimbus-7* and using 850 mb cloud drift winds as u_e, satisfactorily estimated E-P in the tropical Pacific. The top of the boundary layer is approximately 850 mb, and the wind at this level is closely related to surface level wind through similarity relations (e.g., Brown and Liu 1982). In the past, oceanographers used to get ocean surface wind stress by multiplying the geostrophic winds (derived from pressure gradient) by a constant factor and tuning them by a constant angle. Statistical models between u_e and u_s have been developed from a combination of NCEP wind and humidity profiles over oceans and the global radiosonde network, using both multivariate regression and neural network. The method is able to capture both high- and low-frequency variations of u_e, as validated with time series of global radiosonde stations (Liu and Tang 2005).

The Atlantic influence on rainfall over eastern Brazil at intraseasonal time scales is clearly shown in Figure 5-5. During the wet phase, as defined by the high values of the rainfall time series, strong Brazilian rain is in phase with two strong cyclones in the subtropical Atlantic, with onshore moisture advection across the north coast.
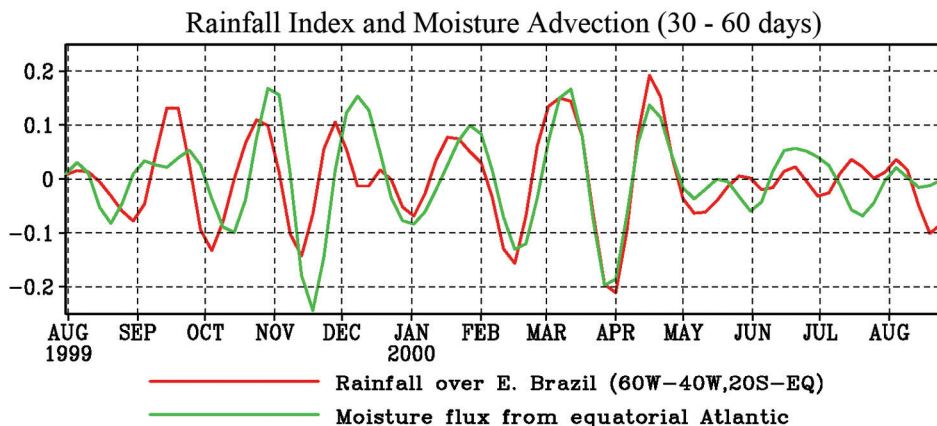

Figure 5-5   Time series of 30–60 day bandpass-filtered rainfall over eastern Brazil derived from TRMM and integrated moisture transport across Atlantic coastline of northern Brazil.

5.8.4   El Niño and Multi-scale Interaction

El Niño and Southern Oscillation (ENSO), the strongest interannual climatic signal, is believed to be associated with the collapse of the trade winds in the equatorial Pacific. El Niño is usually preceded by an increase in intensity and frequency of westerly wind anomalies in the central equatorial Pacific (e.g., Luther et al. 1983). Scatterometers have revealed, with unprecedented resolution, the evolution of the tropical wind systems associated with ENSO. Liu et al. (1995) related the westerly wind anomalies in the western Pacific observed by the ERS scatterometer to the propagation of Kelvin waves across the Pacific and sea level changes observed by the TOPEX/Poseidon altimeter, and the subsequent ocean warming and increase in atmospheric water vapor observed by spaceborne radiometers. Using ERS wind forcing, they were able to simulate the sea level and sea surface temperature changes using an OGCM. Before El Niño, the westerly wind bursts (WWB) were also associated with twin cyclones, moving north and south from the equator (e.g., Keen 1982). The near-real-time access of QuikSCAT data advanced the monitoring of the changes in trade winds and the spawning of the twin cyclones. An example of strong westerly winds along the equator and the twin cyclones observed by QuikSCAT is shown in Figure 5-6. Yu et al. (2003) put forth a hypothesis, also based on scatterometer winds, that the WWBs are part of the ENSO dynamics rather than external stochastic forcing. Liu et al. (1998b) were also able to show winds as the possible atmospheric bridge that connected synoptic-scale WWBs with interannual ENSO anomalies and their modification to the decadal extratropical dipole, using NSCAT data. The results were in agreement with the long-term simulation of a coupled ocean-atmospheric general circulation model (Yu et al. 2000).
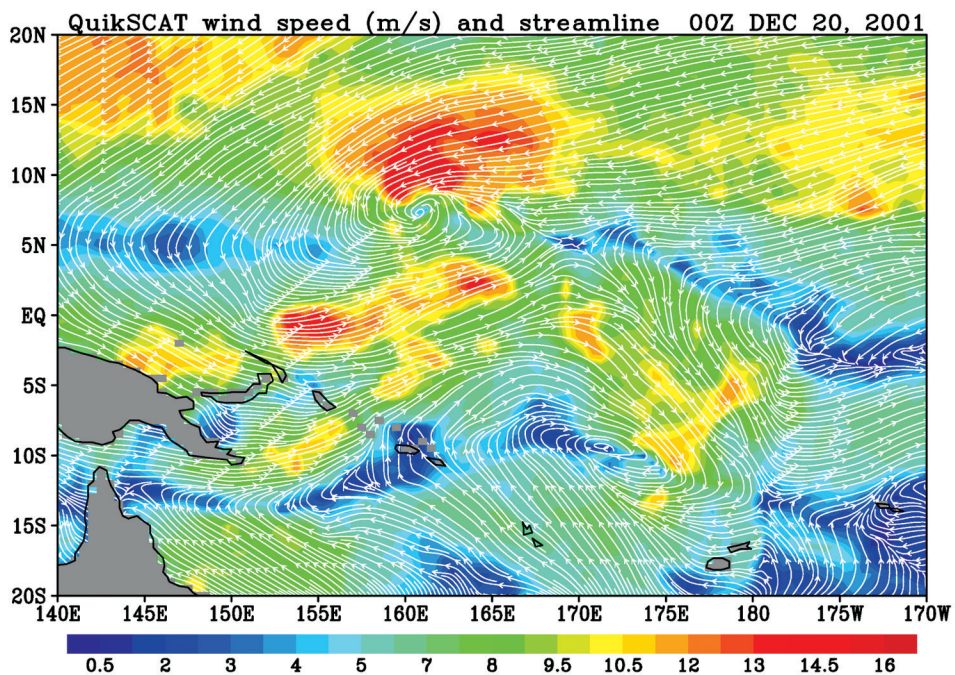

Figure 5-6   Westerly wind burst and twin cyclones observed in near-real-time by QuikSCAT. White arrows representing wind direction are superimposed on color image of wind speed.

5.8.5   Ocean-atmosphere Coupling

The advance of spacebased microwave sensors that measure ocean surface wind vector and SST (Wentz et al. 2000), under both clear and cloudy conditions, night and day, opens new opportunities for studying ocean-atmosphere coupling. The recent improvement in the spatial resolution of scatterometer winds as described in Section 5.5.2 pushes the applications to coastal oceans. Examples of the manifestation of the coupling—the correlation between SST and surface wind—will be discussed as viewed from two perspectives (one with the atmosphere and the other with the ocean as the driving force).

5.8.5.1   WIND FORCING

The ocean will respond to surface wind and thermal forcing by changing SST and dynamic topography, which are observed by spacebased radiometers and altimeters. Liu et al. (1994), using measurements by the SSM/I, clearly demonstrated a negative lag correlation between surface winds and SST in annual and interannual time scales over most of the global oceans. High winds increase evaporative cooling, decreasing mixed layer heat content and SST.

Dynamic coupling should be manifested through lag correlations between the curl of wind stress (CWS) and dynamic topography and between CWS and SST. Waves and current advection often obscure direct observations of such simple correlations in open oceans. South China Sea (SCS) is semi-enclosed, where such negative lag correlations were observed in annual time scales using only spacebased data (Liu and Xie 1999). In the center of the SCS basin, the winter monsoon causes positive CWS (cyclonic circulation), divergence of surface water, upwelling of cold water, and depression of sea level and SST. The summer monsoon, with negative CWS, causes opposite responses. During summer the anticyclone circulation in the center of the basin is punctuated by a wind jet branching off from the South Vietnamese coast, causing positive CWS and low sea level and SST two months later. It has been suggested that the wind jet is influenced by the land topography of South Vietnam (Xie et al. 2003).

In shorter time scales, Lin et al. (2003b) observed a strong decrease of SST after the passage of a tropical cyclone in SCS, which is largely caused by wind-driven Ekman pumping and vertical mixing in the ocean. Such cooling was also simulated by numerical models in the same areas (Chu et al. 1999).

5.8.5.2   OCEAN FORCING

Liu and Xie (2002), in their study of the double intertropical convergence zone (ITCZ), presented observational evidence of two major mechanisms by which the ocean drives the atmosphere. When the ocean is warm and SST is above the deep convection threshold (around 26–27°C), surface winds from different directions converge to the local SST maximum, driven by the pressure gradient force. The local maxima of wind convergence and SST are approximately collocated. The stronger ITCZ occurs when the northerly trade winds meet the southerly trade winds over warm water. The weaker ITCZ occurs over cooler water and is caused by the deceleration of the surface winds as they approach the cold upwelling water near the equator. Decreases in vertical mixing and increases in vertical wind shear in the atmospheric boundary layer are suggested to be the causes of the deceleration of the trade winds as they move from warmer to colder water.

The relation between wind shear and atmospheric density stratification (stability) has been well known and discussed in turbulence transfer textbooks. A review on atmospheric stability driven by wind shear and buoyancy is given by Liu et al. (1979) and others. The change in wind shear in the boundary layer was used by Xie et al. (1998) to explain the coherence between SST and surface wind in the tropical instability waves (TIW)—the

westward-propagating temperature front of the cold tongue. Liu et al. (2000b) validated this model with rawinsonde measurements of a research cruise across the TIW, and with the phase difference between spacebased wind and SST measurements. Surface wind convergence is at quadrature with SST. The two mechanisms were further examined by Chelton et al. (2001) and Hashizume et al. (2002).

Similar ocean-driven coupling over cool water, which results in positive contemporary correlation between wind speed and SST, appears to be much more prevalent. It was observed in the cold patches behind typhoon passages (Lin et al. 2003c) and even over Gulf Stream rings (Park and Cornillon 2002).

The ocean-driven coupling is evident during winter and spring in the vicinity of East China Sea. Xie et al. (2002) showed a strong warm tongue stretching from Cheju Island off the coast of South Korea, through the Yellow Sea to the Bohai Bay. It is separated from a similar warm tongue in East China Sea to the south by a cold tongue. They showed that the warm and cold tongues are collocated with high and low winds in the East China Sea, but the convergences are located at the front where the SST gradient is strongest. There is a strong wind jet blowing along the Kuroshio front, most probably driven by a cross-front pressure gradient. The location of convergence with respect to the SST fronts reveals the role played by the two mechanisms. Chen et al. (2003) simulated the ocean circulation cell and biological pumping associated with this frontal wind jet using a coupled model.

5.9   FUTURE TECHNOLOGY

One of the drawbacks of present scatterometers is the wind-direction ambiguity. The backscatter is a cosine function of the azimuth angle. In a recent experiment, it was demonstrated that the correlation between co-polarized and cross-polarized backscatter is a sine function of azimuth angle. By adding a receiver of cross-polarized backscatter to the scatterometer on QuikSCAT, the directional ambiguity problem can be mitigated (Tsai et al. 2000). Although QuikSCAT has a continuous scan, the azimuth angles are too close together at the outer swath and too far apart near nadir, hampering selection of wind direction. With polarimetric scatterometers, uniform retrieval accuracy across the entire swath can be achieved. For future scatterometers, the potential is being explored of adding polarimetric radiometers (see Section 5.7) with different wind-direction aliasing characteristics.

The accuracy of wind detection from the higher resolution "sliced" data, as discussed in Section 5.5.2, can be improved by changing the design of future scatterometers to increase the signal-to-noise ratio. This could be achieved by slightly increasing the size of the antenna and the emitting power. QuikSCAT is a real-aperture system, which employs only a range-discrimination technique, and the spatial resolution is limited by the antenna size. The present instrument uses a 1-m antenna. A larger antenna (2 m) will greatly enhance the spatial resolution. Another way to achieve higher resolution is to add synthetic aperture capability to discriminate the illuminated scene in both range and Doppler, as proposed by Spencer et al. (2003) and others.

Historically, ESA used the C-band (5 GHz), but NASA preferred the Ku-band (14 GHz). Since a higher frequency is more sensitive to shorter surface waves, the Ku-band is more sensitive to wind variation at low winds, but is more subject to atmospheric attenuation effects and rain contamination. There have been suggestions for more than a decade for a multi-frequency scatterometer that is sensitive to various parts of the ocean surface wave spectrum (e.g., Huang et al. 1984). Such a scatterometer may mitigate the shortcomings of both C-band and Ku-band scatterometers.

5.10 EXTENDED TIME SERIES

Consistent and continuous long-time series of ocean wind vectors is needed for the study of climate changes. A series of C-band scatterometers, ASCAT, is planned on METOP, starting in 2006, to give operational data of ocean surface wind vectors, but the spatial resolution and coverage of ASCAT are not as good as SeaWinds. Polarimetric radiometers, starting with WindSAT and continuing to CMIS on NPOESS, have the advantage of requiring less money to build and less electrical power to operate. However, the accuracy of this new technique has not been quantified. Such radiometers may not have sufficient sensitivity to wind direction at low winds (< 7 m/s) and under cloudy or light-rain conditions. The original plan of continuous long duration of wind vectors from Ku-band scatterometers on a series of three ADEOS satellites was cut short by premature failures of the spacecraft. An advanced scatterometer with uninterrupted wide-swath, enhanced spatial resolution, and polarimetric capability to mitigate wind directional ambiguity is needed after QuikSCAT, to prevent degrading the quality of future wind vector data and to meet the generally quoted requirements of 1-km and 6-hour resolutions for both the scientific and operational communities.

5.11 ACKNOWLEDGEMENTS

References

Alpers, W. and H. Huhnerfuss. 1989. The damping of ocean waves by surface films: A new look at an old problem. *J. Geophys. Res*. 94:6251–6265.

Atlas, R. S., R. N. Hoffman, S. C. Bloom, J. C. Jusem, and J. Ardizzone. 1996. A multiyear global surface wind velocity data set using SSM/I wind observations. *Bull. Amer. Meteor. Soc.* **77**:869–882.

Atlas, R., R. N. Hoffman, S. M. Leidner, J. Sienkiewicz, T.-W. Yu, S. C. Bloom, E. Brin, J. Ardizzone, J. Terry, D. Bungato, and J.C. Jusem. 2001. The effects of marine winds from scatterometer data on weather analysis and forecasting. *Bull. Amer. Meteor. Soc*. 82:1965–1990.

Barger, W. R., W. D. Garrett, E. Mollo-Christensen, and K. W. Ruggles. 1970. Effects of an artificial slick upon the atmosphere and the ocean. *J. Appl. Meter*. 9:396–400.

Barrick, D. E. 1974. Wind dependence of quasi-specular microwave sea scatter. *IEEE Trans. Antennas Propag*. AP-22:1135.

Boukabara, S.-A., R. N. Hoffman, C. Grassotti, and S. Mark Leidneer. 2002. Physically based modeling of QuikSCAT SeaWinds passive microwave measurements for rain detection. *J. Geophys. Res*. 107, D22:4786, doi:10.1029/2001JD001243.

Brown, R. A. 1970. A secondary flow model for the planetary boundary layer. *J. Atmos. Sci*. 27:742–757.

———. 2000. On satellite scatterometer model functions. *J. Geophys. Res.* 105:29195–29205.

———. 2002. Scaling effects in remote sensing applications and the case of organized large eddies. *Can. J. Remote Sensing* 28, no. 3:340–345.

Brown, R. A. and W. T. Liu. 1982. An operational large-scale marine planetary boundary layer model. *J. Appl. Meteor*. 2:261–269.

Brown, R. A. and L. Zeng. 2001. Comparison of planetary boundary layer model winds with dropsonde observations in tropical cyclone. *J. Appl. Meteor*. 40:1718–1723.

Brown, G. S., H. R. Stanley, and N. A. Roy. 1981. The wind speed measurement capability of space-borne radar altimeters. *IEEE J. Oceanic Eng*. OE-6(2):59–63.

Bryan, E. and A. Oort. 1984. Seasonal variation of the global water balance based on aerological data. *J. Geophys. Res*. 89:11717–11730.

Busalacchi, A. J., R. M. Atlas, and E. C. Hackert. 1993. Comparison of special sensor microwave imager vector wind stress with model-derived and subjective products for the tropical Pacific. *J. Geophys. Res*. 98:6961–6977.

Carter, D.J.T., P. G. Challenor, and M. A. Srokosz. 1992. An assessment of Geosat wave height and wind speed measurements. *J. Geophys. Re*s. 97:11383.

Chelton, D. B. and P. J. McCabe. 1985. A review of satellite altimeter measurement of surface wind speed: With a proposed new algorithm. *J. Geophys. Res*. 90:4707–4720.

Chelton, D. B. and F. J. Wentz. 1986. Further development of an improved altimeter wind speed algorithm. *J. Geophys. Res*. 91:14150–14260.

Chelton, D. B., S. K. Esbensen, M. G. Schlax, N. Thum, M. H. Freilich, F. J. Wentz, C. L. Gentemann, M. J. McPhaden, and P. S. Schoff. 2001. Observations of coupling between surface wind stress and sea surface temperature in the eastern tropical Pacific. *J. Climate* 14:1479–1498.

Chen, D., W. T. Liu, W. Tang, and Z. Wang. 2003. Air-sea interaction at an oceanic front: Implications for frontogenesis and primary production. *Geophys. Res. Lett.* 30, no. 14:1745, doi:10.1029/2003GL017536.

Chu, P. C., S. Lu, and W. T. Liu. 1999. Uncertainty of South China Sea prediction using NSCAT and National Centers for Environmental Prediction winds during tropical storm Ernie, 1996. *J. Geophys. Res.* 104, C5:11273–11289.

Clemente-Colon, P. and X.-H.Yan. 1999. Observations of east coast upwelling conditions in synthetic aperture radar imagery. *IEEE Trans. Geosci. Remote Sens*. 37:2239–2248.

Cornillon, P. and K.-A. Park. 2001. Warm core ring velocities inferred from NSCAT. *Geophys. Res. Lett*. 28:575–578.

Davis, S. R. 2002. Some impacts of SeaWinds data in numerical weather prediction. M.S. Thesis. Florida State University, Tallahassee.

Dobson, E., F. Monaldo, J. Goldhirsh, and J. Wikerson. 1987. Validation of Geosat altimeter derived wind speeds and significant wave heights using buoy data. *J. Geophys. Res*. 92:10719–10731.

Donelan, M. A. and W. J. Pierson. 1987. Radar scattering and equilibrium ranges in wind-generated waves with application to scatterometry. *J. Geophys. Res*. 92:4971–5029.

Donnelly, W. J., J. R. Carswell, R. E. McIntosh, P. S. Chang, J. Wilkerson, F. Marks, and P. G. Black. 1999. Revised ocean backscatter models at C and Ku band under high-wind conditions. *J. Geophys. Res*. 104:11485–11497.

Ebuchi, N. 1997. Sea surface temperature dependence of C-band radar cross sections observed by ERS-1/AMI scatterometer. *J. Adv. Mar. Sci. Tech. Soc*. 3:157–168.

Figa-Saldana, J., J.J.W. Wilson, E. Attema, R. Gelsthorpe, M. R. Drinkwater, and A. Stoffelen. 2002. The advanced scatterometer (ASCAT) on the meteorological operational (MetOp) platform: A follow on for European wind scatterometers. *Can. J. Remote Sens*. 28:404–412.

Fu, L.-L., ed. 2003. Wide-swath altimetric measurement of ocean surface topography. *JPL Publ. 03-002*. Pasadena, Calif.: Jet Propulsion Laboratory.

Gade, M., W. Alpers, H. Huhnerfuss, V. R. Wismann, and P. A. Lange. 1998. On the reduction of the radar backscatter by oceanic surface films: Scatterometer measurements and their theoretical interpretation. *Remote Sens. Environ*. 66:52–70.

Gerling, T. W. 1986. Structure of the surface wind field from the Seasat SAR. *J. Geophys. Res*. 91:2308–2320.

Glazman, R. E. and A. Greysukh. 1993. Satellite altimeter measurements of surface wind. *J. Geophys. Res*. 98:2475–2483.

Glazman, R. E. and S. Pilorz. 1990. Effects of sea maturity on satellite altimeter measurements of surface wind. *J. Geophys. Res*. 95:2857–2870.

Gonzales, A. E. and D. G. Long. 1999. An assessment of NSCAT ambiguity removal. *J. Geophys. Res*. 104:11449–11457.

Goodberlet, M. A. and C. T. Swift. 1989. Remote sensing of ocean surface winds with the special sensor microwave/imager. *J. Geophys. Res*. 94:13547–14555.

Gower, J.F.R. 1996. Intercalibration of wave and wind data from Topex/Poseidon and moored buoys off the west coast of Canada. *J. Geophys. Res*. 101:3817–3830.

Hashizume, H. and W. T. Liu. 2004. Systematic error of microwave scatterometer wind related to the basin-scale plankton bloom. *Geophys. Res. Lett.* 31, L06307, doi:10.10219/ 2003GTL01841.

Hashizume, H., S.-P.Xie, M. Fujiwara, M. Shiotani, T. Watanabe, Y. Tanimoto, W.T. Liu, and K. Takeuchi. 2002. Direct observations of atmospheric boundary layer response to slow SST variations over the eastern equatorial Pacific. *J. Climate* 15:3379–3393.

Heta, Y. and Y. Mitsuta. 1993. An evaluation of evaporation over the tropical Pacific Ocean as observed from satellites. *J. Appl. Meteor*. 32:1242–1247.

Hollinger, J. P. 1971. Passive microwave measurements of sea surface roughness. *IEEE Trans. Geosci. Electronics* GE-9:165–169.

Hu, H. and W. T. Liu. 2002. QuikSCAT reveals the surface circulation of Catalina Eddy. *Geophys. Res. Lett.* 29, no. 17:1821, doi:10.1029/ 2001GL014203.

———. 2003. Oceanic thermal and biological responses in Santa Ana winds. *Geophys. Res. Lett.* 30, no. 11:1596, doi:10.1029/2003GL017159.

Huang, N. E., C. L. Parsons, S. R. Long, and L. F. Bliven. 1984. A new type of overshoot phenomenon in wind wave development and its implications in remote sensing of the ocean. *J. Geophys. Res*. 89:3679–3687.

Huddleston, J. N. and B. W. Stiles. 2000. A multi-dimensional histogram rain flagging technique for SeaWinds on QuikSCAT. *Proc. of IGARSS Conference*, Vol. 3, 1232–1234, IEEE.

Huhnerfuss, H., W. Alpers, and W. L. Jones. 1978. Measurements at 13.9 GHz of the radar backscattering cross section of the North Sea covered with an artificial surface film. *Radio Sci.* 13:979–983.

Hwang, P. A., W. J. Teague, G. A. Jacobs, and D. W. Wang. 1998. A statistical comparison of wind speed, wave height and wave period derived from satellite altimeters and ocean buoys in the gulf of Mexico region. *J. Geophys. Res*. 103:10451–10468.

Jones, W. L., F. J. Wentz, and L. C. Schroeder. 1978. Algorithm for inferring wind stress from SEASAT-A. *J. Spacecraft and Rockets* 15:368–374.

Jones, W. L., T. Kasparis, Y. Wang, and J. Park. 2001. Global ocean rain rates from QuikSCAT. *7th International Conf. on Precipitation*. 30 June–3 July, Samoset Resort, Rockport, Maine.

Katsaros, K. B., P. W. Vachon, and W. T. Liu. 2002. Remote sensing of tropical cyclones from space. *J. Oceanogr*. 58:137–151.

Katsaros, K. B., P. W. Vachon, P. G. Black, P. P. Dodge, and E.W. Uhlhorn. 2000. Wind fields from SAR: Could they improve our understanding of storm dynamics? *John Hopkins APL Technical Digest* 21, no. 1:86–93.

Keen, R. A. 1982. The role of cross-equatorial tropical cyclone pairs in the Southern Oscillation. *Monthly Weather Review* 110:1405–1416.

Keller, W. C., V. Wismann, and W. Alpers. 1989. Tower-based measurements of the ocean C band radar backscattering cross section. *J. Geophys. Res.* 94:924–930.

Kelly, K. A., S. Dickensen, M. J. McPhaden, and G. C. Johnson. 2001. Ocean currents evident in satellite wind data. *Geophys. Res. Lett*. 28:2469–2472.

Korsbakken, E., J. A. Johannessen, and O. M. Johannessen. 1998. Coastal wind field retrievals from ERTS synthetic aperture radar images. *J. Geophys. Res.* 103:7857–7874.

Krishen, K. 1973. Detection of oil spills using a 13.3-GHz radar scatterometer. *J. Geophys. Res*. 78:1952–1963.

Lefevre, J. M., J. Vbarckicke, and Y. Ménard. 1994. A significant wave height and radar cross section to improve radar altimeter measurements. *J. Geophys. Res*. 99:25035–25046.

Lehner, S., J. Horstmann, W. Koch, and W. Rosenthal. 1998. Mesoscale wind measurements using recalibrated ERS SAR images. *J. Geophys. Res.* 103:7847–7856.

Lin, I-I, L.-S. Wen, K.-K. Liu, W.-T. Tsai, and A. K. Liu. 2002. Evidence and quantification of the correlation between radar backscatter and ocean colour supported by simultaneously acquired in situ sea truth. *Geophys. Res. Lett*. 29, no. 10:1464, doi:10.1029/2001GL014039.

Lin, I-I, W. Alpers, and W. T. Liu. 2003a. First evidence for the detection of natural surface films by the QuikSCAT scatterometer. *Geophys. Res. Lett.* 30, no. 13:1713, doi:10.1029/ 2003GL017415.

Lin, I-I, W. T. Liu, C.-C. Wu, G.T.F. Wong, C. Hu, Z. Chen, W.-D. Liang, Y. Yang, and K.-K. Liu. 2003b. New evidence for enhanced ocean primary production triggered by tropical cyclone. *Geophys. Res. Lett.* 30, no. 13:1718, doi:10.1029/2003GL017141.

Lin, I.-I., W. T. Liu, C.-C. Wu, J. C. Chiang, and C.-H. Sui. 2003c. Satellite observations of modulation of surface winds by typhoon-induced upper ocean cooling. *Geophys. Res. Lett.* 30, no. 3:1131, doi:10.1029/2002GL015674.

Liu, A. K., W. G. Pichel, W. Y. Tseng, and S. Y. Wu. 2000. Wavelet analysis of SAR images for coastal monitoring. *Can. J. Remote Sens.* 26:494–499.

Liu, W. T. 1984. The effects of the variations in sea surface temperature and atmospheric stability in the estimations of average wind speed by Seasat-SASS. *J. Phys. Oceanogr.* 14:392-401.

———. 1987. El Niño Atlas, Nimbus-7 microwave radiometer data. *JPL Publication 87-5*. Pasadena, Calif.: Jet Propulsion Laboratory.

———. 1993. Ocean surface evaporation. Pages 265–278 in *Atlas of Satellite Observations Related to Global Change*. Edited by R. J. Gurney, J. Foster, and C. Parkinson. Cambridge, UK: Cambridge University Press.

———. 2002. Progress in scatterometer application. *J. Oceanogr.* 58:121–136.

———, ed. 2003. Scientific opportunities provided by SeaWinds in tandem. *JPL Publication 03-12*. Pasadena, Calif.: Jet Propulsion Laboratory.

Liu, W. T. and W. G. Large. 1981. Determination of surface stress by Seasat-SASS: A case study with JASIN data. *J. Phys. Oceanogr.* 11:1603–1611.

Liu, W. T. and W. Tang. 1996. Equivalent neutral wind. *JPL Pub. 96-17*. Pasadena, Calif.: Jet Propulsion Laboratory.

———. 2005. Estimating moisture transport over ocean observed from space. *J. Geophys. Res.* 110, D10101, doi:10.1029/2004JD005300.

Liu, W. T. and X. Xie. 1999. Spacebased observations of the seasonal changes of South Asian monsoons and oceanic responses. *Geophys. Res. Lett.* 26, no. 10:1473–1476.

———. 2002. Double intertropical convergence zones – A new look using scatterometer. *Geophys. Res. Lett.* 29, no. 22:2072, doi:10.1029/2002GL015431.

Liu, W. T., K. B. Katsaros, and J. A. Businger. 1979. Bulk parameterization of air-sea exchanges in heat and water vapor including the molecular constraints at the interface. *J. Atmos. Sci.* 36:1722–1735.

Liu, W. T., W. Tang, and P. P. Niiler. 1991. Humidity profiles over ocean. *J. Climate* 4:1023–1034.

Liu, W. T., W. Tang, and L. L. Fu. 1995. Recent warming event in the Pacific may be an El Nino. *Eos Trans of Amer. Geophys. Union* 76:429–437.

Liu, W. T., W. Tang, and R. Atlas. 1996. Responses of the tropical Pacific to wind forcing as observed by spaceborne sensors and simulated by an ocean general circulation model. *J. Geophys. Res.* 101:16345–16359.

Liu, W. T., W. Tang, and P. S. Polito. 1998a. NASA scatterometer provides global ocean-surface wind fields with more structures than numerical weather prediction. *Geophys. Res. Lett.* 25:761–764.

Liu, W. T., W. Tang, and H. Hu. 1998b. Spaceborne sensors observe various effects of anomalous winds on sea surface temperatures in the Pacific Ocean. *Eos Trans. Amer. Geophys. Union* 79:249, 252.

Liu, W. T., A. Zhang, and J.K.B. Bishop. 1994. Evaporation and solar irradiance as regulators of sea surface temperature in annual and interannual changes. *J. Geophys. Res.* 99, C6:12623–12637.

Liu, W. T., H. Hu, and S. Yueh. 2000a. Interplay between wind and rain observed in Hurricane Floyd. *Eos Trans. of Amer. Geophys. Union* 81:253, 257.

Liu, W. T., X. Xie, P. S. Polito, S. Xie, and H. Hashizume. 2000b. Atmosphere manifestation of tropical instability waves observed by QuikSCAT and tropical rain measuring missions. *Geophys. Res. Lett.* 27:2545–2548.

Liu, W.T., H. Hu, Y. T. Song, and W. Tang. 2001. Improvement of scatterometer wind vectors – Impact on hurricane and coastal studies. *Proc. WCRP/SCOR Workshop on Intercomparison and Validation of Ocean-Atmosphere Flux Fields.* WCRP-115, World Climate Research Programme, Geneva, 197–200.

Lleonart, G. T. and D. R. Blackman. 1980. The spectral characteristics of wind-generated capillary waves. *J. Fluid Mech.* 97:445–479.

Lo, R.C.A. 1983. A comprehensive description of the missing sensor microwave imager SSM/I environmental parameter extraction algorithm. *NRL Memo Rep. 5199.* Washington, D.C.: Nav. Res. Lab.

Long, David. 2001. Personal communication.

Long, D. G., P. J. Hardin, and P. T. Whiting. 1993. Resolution enhancement of spaceborne scatterometer data. *IEEE Trans. Geosci. Remote Sens.* 31, no. 3:700–715.

Luther, D. S., D. E. Harrison, and R. A. Knox. 1983. Zonal winds in the central equatorial Pacific. *Science* 222:327–330.

Mears, C. A., D. K. Smith, and F. J. Wentz. 2001. Comparison of special sensor microwave imager and buoy-measured wind speeds from 1987 to 1997. *J. Geophys. Res*. 106:11719–11729.

Meissner, T., D. Smith, and F. Wentz. 2001. A 10-year intercomparison between collocated Special Sensor Microwave Imager oceanic surface wind speed retrievals and global analyses. *J. Geophy. Res*. 106: 11731–11742.

Monaldo, F. and E. Dobson. 1989. On using significant wave height and radar cross section to improve radar altimeter measurements. *J. Geophys. Res*. 94:12699–12701.

Monaldo, F. M., D. R. Thompson, R. C. Beal, W. G. Pichel, and P. Clemente-Colon. 2001. Comparison of SAR- derived wind speed with model predictions and ocean buoy measurements. *IEEE Trans. Geosci. Remote Sens*. 39:2587–2600.

Moore, R. K. and A. K. Fung. 1979. Radar determination of winds at sea. *Proc. IEEE* 67:1504–1521.

Pacanowski, R. C. 1987. Effect of equatorial currents on surface stress. *J. Phys. Oceanogr*. 17:833–838.

Park, K-A. and P. Cornillon. 2002. Stability-induced modification of sea surface winds over Gulf Stream rings. *Geophys. Res. Lett*. 29, no. 24:2211, doi:10.1029/2001GL014236i.

Petoux, J., R. C. Foster, and R. A. Brown. 2003. Global pressure fields from scatterometer winds. *J. Appl. Meteor*. 42:813–826.

Piepmeier, J. R. and A. J. Gasiewski. 2001. High-resolution passive polarimetric microwave mapping of ocean surface wind vector fields. *IEEE Trans. Geosci. Remote Sensing* 39, no. 3:606–622.

Pierson, W. J. 1983. Highlights of the SEASAT-SASS program: A review. Chapter 4, pages 69–86 in *Satellite Microwave Remote Sensing*, edited by T. D. Allan. Chichester: Ellis Horwood Ltd.

Plant, W. J. 1990. Bragg scattering of electromagnetic waves from the air/sea interface. Chapter 11, pages 41–108 in *Surface Waves and Fluxes*, *Vol. II-Remote Sensing*. Edited by G. L. Geernaert and W. J. Plant. Dordrecht, Holland: Kluwer Academic Publishers.

Polito, P. S., J. P. Ryan, W. T. Liu, and F. P. Chavez. 2001. Oceanic and atmospheric anomalies of tropical instability waves. *Geophys. Res. Lett*. 28:2233–2236.

Portabella, M. and A. Stoffelen. 2002. A comparison of KNMI quality control and JPL rain flag for SeaWinds. *Can. J. Remote Sens*. 28, no. 3:424–430.

Quilfen, Y., B. Chapron, and D. Vandemark. 2001. The ERS scatterometer wind measurement accuracy: Evidence of seasonal and regional biases. *J. Atmos. Oceanic Tech*. 18:1684–1697.

Ritchie, E., J. Simpson, W. T. Liu, C. Veldon, K. Brueske, and J. Halvorsen. 2002. A closer look at hurricane formation and intensification using new technology. Chapter 12, pages 249–290 in *Coping with Hurricanes*. Edited by R. Simpson, M. Garstang, and R. Anthes. Washington, D.C.: Amer. Geophys. Union.

Shaffer, S. J., R. S. Dunbar, S. V. Hsiao, and D. G. Long. 1991. A median-filer-based ambiguity removal algorithm for NSCAT. *IEEE Trans. Geosci. Remote Sens*. 29:167–174.

Skou, N. and B. Laursen. 1998. Measurement of ocean wind vector by an airborne, imaging polarimetric radiometer. *Radio Sci*. 33, no. 3:669–675.

Sobieshi, P. W. and L. F. Bliven. 1995. Scatterometry of a drop impact on a salt-water surface. *Int. J. Remote Sens*. 16, no. 14:2721–2726.

Spencer, M. W., C. Wu, and D. G. Long. 2000. Improved resolution backscatter measurements with the SeaWinds pencil-beam scatterometer. *IEEE Trans. Geosci. Remote Sens*. 38:89–104.

Spencer, M. W., W.-Y. Tsai, and D. G. Long. 2003. High-resolution measurements with a spaceborne pencil-beam scatterometer combined range/doppler discrimination techniques. *IEEE Trans. Geoscience Remote Sensing* 41, no. 3:567–581.

Stiles, B. W. and S. H. Yueh. 2002. Impact of rain on spaceborne Ku-band wind scatterometer data. *IEEE Trans. Geosci. Remote Sens*. 40:1973–1983.

Stoffelen, A. and D. Anderson. 1997. Scatterometer data interpretation: Estimation and valida-tion of the transfer function CMOD4. *J. Geophys. Res*. 102:5767–5780.

Tang, W., B. Stiles, and W. T. Liu. 2004. Evaluation of high resolution ocean surface vector winds measured by QuikSCAT in coastal region. *IEEE Trans. Geosci. Remote Sens*. 42:1762–1769.

Thompson, T. W., W. T. Liu, and D. E. Weissman. 1983. Synthetic aperture radar observation of ocean roughness from roll in unstable marine boundary layer. *Geophys. Res. Lett*. 10:1172–1175.

Tsai, W.-Y., S. Nghiem, J. Huddelston, M. Spencer, B. Stiles, and R. West. 2000. Polarimetric scatterometer: A promising technique for improving ocean surface measurements from space. *IEEE Trans. Geosci. Remote Sensing* 38:1903–1921.

Vachon, P. W. and F. W. Dobson. 1996. Validation of wind vector retrieval from ERS-1 SAR images over the ocean. *Global Atmos. Ocean System* 5:177–187.

Weissman, D. E. and H. C. Graber. 1999. Satellite scatterometer studies of ocean surface stress and drag coefficient direct model. *J. Geophys. Res*. 104, C5:11329–11335.

Weissman, D. E., M. A. Bourassa, and J. Tongue. 2002. Effects of rain-rate and wind magnitude on SeaWinds scatterometer wind speed errors. *J. Atmos. Oceanic Technol*. 19:738–746.

Wentz, F. J. 1983. A model function for ocean microwave brightness temperatures. *J. Geophys. Res*. 88: 1892–1908.

———. 1992. Measurement of oceanic wind vector using satellite microwave radiometers. *IEEE Trans. Geoscience Remote Sens.* 30, no. 5:960–972.

———. 1997. A well calibrated ocean algorithm for SSM/I. *J. Geophys. Res*. 102:8702–9718.

Wentz, F. J. and D. K. Smith. 1999. A model function for the ocean-normalized radar cross-section at 14 GHz derived from NSCAT observations. *J. Geophys. Res.* 104:11449–11514.

Wentz, F. J., C. L. Gentemann, D. Smith, and D. Chelton. 2000. Satellite measurements of sea surface temperature through clouds. *Science* 288:847–850.

Wentz, F. J., D. K. Smith, C. A. Mears, and C. L. Gentemann. 2001. Advanced algorithm for QuikSCAT and SeaWinds/AMSR. *Proc. of IGARSS 2001*, IEEE.

Wilheit, T. T. 1979. A model for the microwave emissivity of the ocean's surface as a function of wind speed. *IEEE Trans. Geoscience Electronics* GE-17:244–249.

Wilheit, T. T. and A. T. Chang. 1980. An algorithm for retrieval of ocean surface and atmospheric parameters from the observations of the scanning multichannel microwave radiometer. *Radio Sci.* 15:525–544.

Witter, D. L. and D. B. Chelton. 1991. A geosat altimeter wind speed algorithm and a method from altimeter wind speed algorithm development. *J. Geophys. Res*. 46:8853–8860.

Wu, J. 1991. Effects of atmospheric stability on ocean ripples: A comparison between optical and microwave measurements. *J. Geophys. Res*. 96:7265–7269.

Xie, S.-P., M. Ishiwatari, H. Hashizume, and K. Takeuchi. 1998. Coupled ocean-atmosphere waves on the equatorial front. *Geophys. Res. Lett.* 25:3863–3866.

Xie, S.-P., Q. Xie, D. Wang, and W. T. Liu. 2003. Summer upwelling in the South China Sea and its role in regional climate variations. *J. Geophys. Res.* 108, C8:3261, doi:10/1029, 2003JC001867.

Xie, S.-P., J. Hafner, Y. Tanimoto, W. T. Liu, H. Tokinaga, and H. Xu. 2002. Bathymetric effect on the winter climate through the sea surface temperature in the Yellow and East China Seas. *Geophys. Res. Lett.* 29, no. 24:2288, doi:10.1029/2002GL015884.

Yanai, M., S. Esbensen, and J. H. Chu. 1973. Determination of bulk properties of tropical cloud clusters from large-scale heat and moisture budgets. *J. Atmos. Sci.* 30:611–627.

Young, I. R. 1993. An estimate of the Geosat altimeter wind speed algorithm at high wind speeds. *J. Geophys. Res*. 93:20275–20286.

Yu, J. Y., W. T. Liu, and C. R. Mechoso. 2000. The SST anomaly Dipole in the northern subtropical Pacific and its relationship with ENSO. *Geophys. Res. Lett.* 27:1931–1934.

Yu, L., R. A. Weller, and W. T. Liu. 2003. Case analysis of a role of ENSO in regulating westerly wind bursts in the Western Equatorial Pacific. *J. Geophys. Res.* 108, C4:3128, doi:10.1029/2002JC001498.

Yueh, S. H., B. Stiles, and W. T. Liu. 2003. QuikSCAT geophysical model function and winds for tropical cyclones. *IEEE Trans. Geophys. Remote Sens.* 41:2616–2628.

Yueh, S. H., W. J. Wilson, S. J. Dinardo, and F. K. Li. 1999. Polarimetric microwave brightness signatures of ocean wind directions. *IEEE Trans. Geosci. Remote Sens.* 37, no. 2:949–959.

Yueh, S. H., W. J. Wilson, F. K. Li, S. V. Nghiem, and W. B. Ricketts. 1995. Polarimetric measurements of sea-surface brightness temperatures using an aircraft K-band radiometer. *IEEE Trans. Geosci. Remote Sens.* 33, no. 1:85–92.

———. 1997. Polarimetric brightness temperatures of sea surfaces measured with aircraft K- and Ka-band radiometers. *IEEE Trans. Geosci. Remote Sens.* 35:1177–1185.

Yueh, S. H., R. West, F. K. Li, W. Y. Tsai, and R. Lay. 2000. Dual-polarized Ku-band backscatter signatures of hurricane ocean winds. *IEEE Trans. Geosci. Remote Sens.* 38:73–88.

Yueh, S. H., B. Stiles, W.-Y. Tsai, H. Hu, and W. T. Liu. 2001. QuikSCAT geophysical model function for tropical cyclones and application to hurricane Floyd. *IEEE Trans. Geosci. Remote Sens.* 39:2601–2612.

Zeng, L. and R. A. Brown. 1998. Scatterometer observations at high wind speeds. *J. Appl. Meteor.* 37:1412–1420.

Zheng, Q., X.-H. Yan, N. E. Huang, V. Klemas, and J. Pan. 1997. The effect of water temperature on radar scattering from the ocean surface. *Global Atmos. Ocean System* 5:273–294.